

Improved Visible Light Harvesting of WO_3 by Incorporation of Sulfur or Iodine: A Tale of Two Impurities

Alexander J. E. Rettie,[†] Kyle C. Klavetter,[†] Jung-Fu Lin,[‡] Andrei Dolocan,[§] Hugo Celio,[§] Ashioma Ishiekwene,[†] Heather L. Bolton,[†] Kristen N. Pearson,[†] Nathan T. Hahn,[¶] and C. Buddie Mullins^{*,†,§,⊥}

[†]McKetta Department of Chemical Engineering, The University of Texas at Austin, Texas 78712 United States

[‡]Department of Geological Sciences, The University of Texas at Austin, Texas 78712 United States

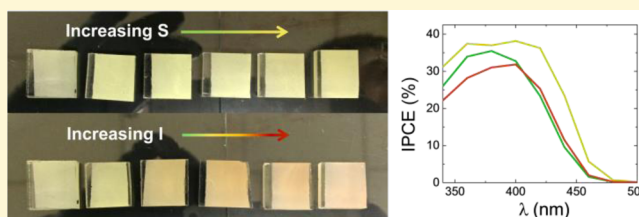
[§]Texas Materials Institute, Department of Mechanical Engineering, The University of Texas at Austin, Texas 78712 United States

[⊥]Center for Electrochemistry, Department of Chemistry, The University of Texas at Austin, Texas 78712 United States

[¶]Sandia National Laboratories, Albuquerque, New Mexico, 87185 United States

Supporting Information

ABSTRACT: We report the incorporation of sulfur or iodine into monoclinic tungsten trioxide (S:WO_3 or I:WO_3 respectively), with the aim to improve its visible light-harvesting ability. Films were synthesized by spray pyrolysis with either ammonium sulfide or iodide added to the aqueous WO_3 precursor solutions. Red shifts of the absorption spectra were observed with S and I incorporation (from ~ 2.7 to 2.6 and 2.1 eV respectively), likely due to the formation of intragap impurity bands. S:WO_3 samples exhibited enhanced photoelectrochemical (PEC) performance at low S concentrations, but this quickly deteriorated with increasing S content. Incident photon conversion efficiency (IPCE) data showed that this initial improvement was driven by improved collection efficiency at longer wavelengths. Conversely, photocurrent decreased at all levels of I addition. IPCE measurements for these films showed only a marginal increase in efficiency at longer wavelengths, indicating that the extra absorbed photons did not contribute significantly to the photocurrent. Time of flight-secondary ion mass spectrometry (ToF-SIMS) depth profiling revealed a uniform distribution of S throughout the S:WO_3 films, but showed surface segregation of I in the I:WO_3 samples. Raman and X-ray photoelectron spectrometry (XPS) showed that S and I substituted for oxygen, but in the case of S, other pathways such as interstitial incorporation and cation substitution could not be ruled out. The complexities of intentionally adding nonmetal impurities to metal oxide systems are highlighted in the context of the existing body of literature.



1. INTRODUCTION

Monoclinic tungsten trioxide (WO_3)¹ is a well-studied photoanode material due to its good charge transport properties and relative stability in acidic electrolytes. These characteristics and modest photocurrents under solar illumination have led to its use in multijunction photoelectrochemical (PEC) systems.^{2–4} However, its band gap of 2.6–2.7 eV limits its solar-to-hydrogen (STH) efficiency for PEC applications to 4–6%, assuming a faradaic efficiency and quantum yield of unity.⁵

Therefore, significant research efforts have been made to increase this material's visible light harvesting ability. The majority of these studies have focused on transition metal^{6,7} or nonmetal doping⁸ and sensitization approaches using dyes⁹ or other semiconductors.^{10–14} Cole et al. investigated nitrogen incorporation in WO_3 thin films, synthesized by reactive RF magnetron sputtering using N_2 as a background gas.¹⁵ Though a significant reduction in the band gap was observed (< 2.0 eV), PEC performance was impaired due to lattice defects. However, other studies where films were treated in ammonia gas to add N

are conflicting, showing improved light absorption and overall PEC performance in some cases¹⁶ but poorer PEC performance in others.¹⁷ Whether these impurities have positive or detrimental effects on the overall photocurrent depends on how they affect the electronic structure of the material, their concentration, and how they are incorporated into the host lattice.

Recent *ab initio*¹⁸ and density functional theory (DFT) studies¹⁹ have indicated that substitution of S at O-sites may create an impurity band that can reduce the band gap of WO_3 . The incorporation of S is relatively unstudied experimentally.²⁰ Additionally, iodine incorporation in TiO_2 particulate photocatalysts has led to improved visible light absorption and photocatalytic activity.²¹ By analogy one may assume that I incorporation may also have a positive effect on WO_3 's visible light absorption. To the best of our knowledge, there are no

Received: December 2, 2013

Revised: January 28, 2014

Published: February 3, 2014

reports on iodine-doped WO_3 . We have developed a simple, scalable spray pyrolysis procedure to synthesize sulfur and iodine-incorporated monoclinic WO_3 (S:WO_3 and I:WO_3 , respectively) films and probe the effects of these impurities on visible light absorption and PEC performance.

First, we characterized the phase and morphology of the samples using X-ray diffraction (XRD) and scanning electron microscopy (SEM). Changes in optical properties were characterized by diffuse reflectance UV–vis spectroscopy. PEC and incident photon conversion efficiency (IPCE) testing were used to evaluate the performance of the films as photoanodes and determine if the extra photons absorbed contributed to the photocurrent. The very low levels of impurities in the samples and their bonding environments were determined by a combination of time-of-flight secondary ion mass spectrometry (ToF-SIMS), X-ray photoelectron spectroscopy (XPS), and Raman spectroscopy. Finally, we discuss and provide evidence for the creation of defect states and their effect on the performance of WO_3 photoanodes.

In the interest of clarity, this report will focus on the 0.1% and 2% S:WO_3 and I:WO_3 films, with data for all doping concentrations in the Supporting Information. These were chosen because the lightly doped films showed the best PEC performance but the smallest change in physical properties and vice versa for the heavily doped films. Further, to avoid repetition, the term “doping” will be used interchangeably with “incorporation” when discussing the addition of S or I to WO_3 .

2. EXPERIMENTAL METHODS

2.1. Synthesis. Films were deposited using a spray pyrolysis setup described previously.^{22,23} Ammonium tungsten oxide hydrate, $(\text{NH}_4)_{10}\text{W}_{12}\text{O}_{41}\cdot 5\text{H}_2\text{O}$ (99.999%, Alfa Aesar), ammonium sulfide, $(\text{NH}_4)_2\text{S}$ (20% in water, Sigma-Aldrich), and ammonium iodide, NH_4I (99%, Acros) were dissolved in demineralized water for use as precursor solutions. The precursor concentration was 0.075 M (based on moles of W), with dopant concentrations added based on the fractional substitution of oxygen (O) sites, that is, a 0.5% doping level corresponds to enough S or I to replace 0.5% of the oxygen sites in fully oxidized WO_3 . Hereafter, samples will be referred to as undoped WO_3 , S:WO_3 , or I:WO_3 with concentrations determined as above. In this study, the concentrations investigated were 0, 0.1, 0.5, 1, 2, and 5% of the total O sites.

Ammonium tungsten oxide hydrate powder was dissolved in demineralized water by stirring for 30 min on a hot plate with a set point of 80 °C. Precursor solutions were pumped intermittently (~10 s on, 25 s off) through an ultrasonic spray nozzle (130 Hz, Sonotech) positioned above a hot plate in a ventilated enclosure under atmospheric conditions. The flow rate was 1.3 mL min^{-1} , the volume per cycle was 0.4 mL, and typically, 25 cycles were required for good coverage of the substrate. Prior to deposition, substrates were ultrasonically cleaned in a mixture of detergent (Contrex), water, and ethanol. After this step they were rinsed in water and ethanol and finally air-dried. The heater temperature set point was 300 °C, resulting in a substrate temperature of ~250 °C during deposition, as measured using an optical pyrometer (Micro-epsilon).

As-deposited films were translucent white and amorphous. Samples were annealed in at 550 °C for 1 h in air and allowed to cool naturally to crystallize the monoclinic phase of WO_3 .

2.2. Compositional Characterization. X-ray diffraction (XRD) was performed using a Philips X'Pert diffractometer

equipped with monochromatic $\text{Cu K}\alpha$ X-rays ($\lambda = 1.54056 \text{ \AA}$). The films were of sufficient thickness to use θ – 2θ scans (without the need for grazing incidence XRD, required for thin films). Film morphology and thickness were determined using a Quanta 650 (FEI) scanning electron microscope (SEM). Diffuse reflectance UV–vis spectra were measured with a Cary 500 spectrophotometer attached to an integrating sphere (Labsphere DRA-CA-5500). X-ray photoelectron spectroscopy (XPS) measurements were performed on a Kratos AXIS Ultra DLD spectrometer with a monochromated $\text{Al K}\alpha$ X-ray source ($h\nu = 1486.5 \text{ eV}$), hybrid optics (employing a magnetic and electrostatic lens simultaneously), and a multichannel plate coupled to a hemispherical photoelectron kinetic analyzer. The photoelectrons takeoff angle was normal to the surface of the sample and 45° with respect to the X-ray beam. An electron flood gun was employed to prevent charging of the samples and the pressure in the analysis chamber was typically 2×10^{-9} Torr during data acquisition. CasaXPS (Version 2.3.15) software was used to analyze the XPS spectra. The adventitious carbon 1s peak was used as a reference with a binding energy (B.E.) of 285 eV. The error in the measurement of the B.E. associated with this procedure varies from ± 0.1 to 0.2 eV.^{24,25} ToF-SIMS data were acquired on a TOF.SIMS 5 instrument (ION-TOF GmbH, Germany, 2010) at a base pressure of $< 2 \times 10^{-9}$ Torr. Elemental concentrations of the species of interest were recorded as function of depth (i.e., depth profiling) by using a pulsed primary ion beam (Bi_1^+ at 30 kV energy and 3 pA measured sample current) for ultrasensitive (parts per billion) surface chemical analysis and a secondary ion beam (Cs^+ at 2 kV energy and 90 nA measured sample current) for sputtering. The depth profiles were acquired in noninterlaced mode (i.e., sequential analysis and sputtering) from an analysis area of $100 \times 100 \mu\text{m}^2$ centered within a previously Cs sputtered $250 \times 250 \mu\text{m}^2$ area. A stable, constant energy (21 eV) electron beam was shot onto the sample surface during data acquisition for charge compensation. All detected secondary ions had negative polarity and with a mass resolution > 5000 ($m/\delta m$). An optical Raman system with a Verdi V2 532 nm green laser, Andor spectrometer, iCCD detector and a 1800 grating was utilized for vibrational spectroscopy measurements. Fityk (Version 0.9.8) peak fitting software was used to analyze the Raman spectra.²⁶

2.3. Photoelectrochemical Testing. Photoelectrochemical measurements were conducted in a glass 3-electrode cell using the WO_3 film as the working electrode, Ag/AgCl (1 M KCl) as the reference electrode, and Pt wire as the counterelectrode. All potentials reported here are versus the reversible H_2 electrode (RHE)

$$E_{\text{RHE}} = E_{\text{Ag}/\text{AgCl}} + 0.059 \times \text{pH} + E_{\text{Ag}/\text{AgCl}}^{\circ} (1\text{M KCl}) \quad (1)$$

where, $E_{\text{Ag}/\text{AgCl}}^{\circ} (1 \text{ M KCl}) = 0.236 \text{ V}$ at 25 °C.²⁷

Illumination was accomplished using a 150 W Xe lamp (Newport) with an AM1.5G filter (Newport) calibrated to 100 mW cm^{-2} using a thermopile. In some experiments a long pass filter (Newport) that only allowed wavelengths greater than 420 nm to pass was added. This decreased the incident power density to 88.5 mW cm^{-2} . A monochromator (Photon Technology International), silicon photodetector (model 818-UV, Newport), and optical power meter (model 1830-C, Newport) were used to determine the incident photon to current conversion efficiency (IPCE). IPCE values were calculated using the formula⁵

$$\text{IPCE}(\lambda) = \frac{1240j(\lambda)}{\lambda P(\lambda)} \times 100 \quad (2)$$

where λ is the wavelength (nm), j is the photocurrent density (mA cm^{-2}), and P is the incident power density of the monochromated light (mW cm^{-2}). Illumination was from the solution-side of the PEC cell in all cases, passing through a glass window and ~ 3 cm of electrolyte solution.

The electrolyte solution used was 1 M methane sulfonic acid (Sigma-Aldrich) with 0.1 M methanol (Fisher) added as a hole scavenger in most cases. A CH Instruments 660D potentiostat was used for all current–voltage and current–time scans. The scan rate was 10 mV s^{-1} .

3. RESULTS AND DISCUSSION

3.1. Synthesis. Extreme care was taken to avoid contamination, as even small concentrations of the dopants studied had large effects on the material's properties. This involved flushing the precursor lines with clean solvent before runs and the use of separate lines for undoped, S:WO₃, and I:WO₃ samples.

Films deposited on quartz substrates were prone to excessive cracking and poor adhesion, whereas deposition on F:SnO₂ on glass (FTO, Pilkington) and glass slides (Corning) resulted in strongly bonded films. Thiourea was tried as an alternative sulfur source to ammonium sulfide, but these films did not adhere strongly to the FTO substrates. Ethanol and ethylene glycol were also candidate solvents but led to poor film coverage.

3.2. Phase and Morphology. X-ray diffraction (XRD) spectra for all samples could only be indexed to monoclinic WO₃ (PDF # 43-1035) and the underlying FTO substrate (Figures S1 and S2 in the Supporting Information), indicating the addition of S or I did not lead to the formation of secondary crystalline phases. At doping levels greater than 2% in the S:WO₃ films, peak broadening was observed, indicative of poorer crystallinity. Although both sulfur and iodine are larger than oxygen and should expand the lattice, the levels of these impurities were too low to induce crystallographic changes detectable by XRD.

Scanning electron microscopy (SEM) revealed a rough, leaf-like microstructure of the WO₃ films grown using spray pyrolysis (Figure 1). Cross-sectional SEM showed that the film thickness after 25 deposition cycles was approximately $5 \mu\text{m}$ but that the film profile was heavily corrugated, with minimum and maximum thicknesses of ~ 3 and $\sim 8 \mu\text{m}$ respectively (Figure 1b). The morphology is attributed to solvent evaporation and particle deposition from the gas phase as the spray approached the hot substrate during synthesis and, similar to other WO₃ films prepared, by spray pyrolysis.^{28,29} The incorporation of S and I did not change the morphology of the WO₃ appreciably (Figure 1c and 1d).

3.3. Optical Properties. For the 2% S:WO₃ and I:WO₃ films, significant color changes were observed relative to the undoped case, from pale green to yellow and brown/red, respectively (Figure 2a). Intermediate compositions exhibited progressive visual color changes (Supporting Information Figure S3) and shifts in absorption spectra (Supporting Information Figures S4 and S5). Tauc plot analyses⁵ yielded indirect transitions at 2.7, 2.6, and 2.1 eV for WO₃, S:WO₃, and I:WO₃, respectively (Supporting Information Figure S6). The addition of sulfur resulted in a slight shift of the absorption edge to longer wavelengths, whereas iodine created what

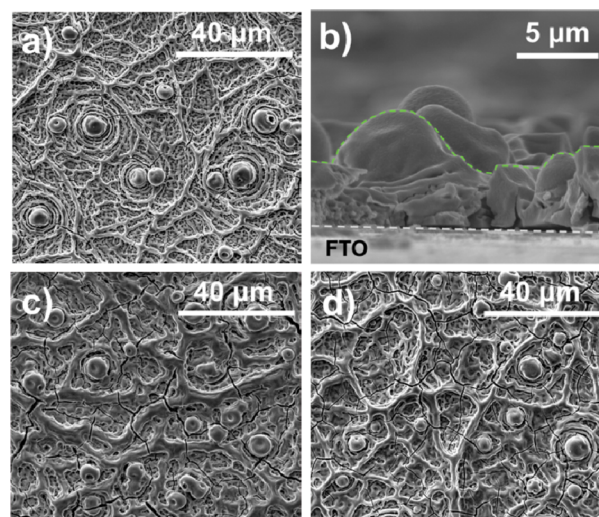


Figure 1. Scanning electron micrographs of the WO₃ film morphology. (a) Undoped WO₃, (b) cross-sectional view of a WO₃ film, (c) 2% S:WO₃, (d) 2% I:WO₃.

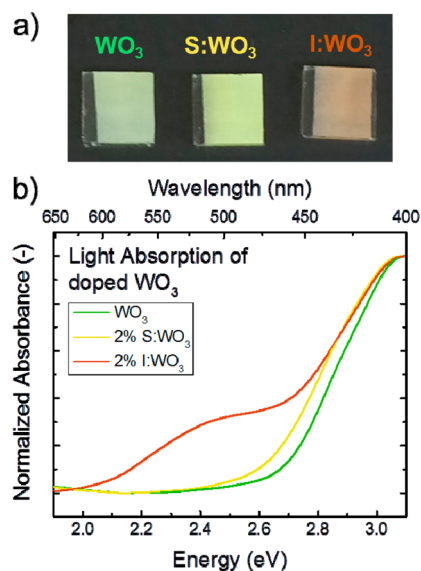


Figure 2. (a) Photograph of undoped, 2% S:WO₃, and 2% I:WO₃ on $1.5 \times 1.5 \text{ cm}^2$ FTO substrates. (b) UV–vis spectra of undoped and doped films.

appeared to be a new and separate transition while retaining the fundamental band gap transition of WO₃ at ~ 2.7 eV (Figure 2b).

We attempted to learn more about these transitions using photoluminescence (PL) spectroscopy, but no PL was observed from the samples at room temperature, indicating that recombination from these new states was nonradiative.

3.4. Photoelectrochemical (PEC) Characterization. The choice of electrolyte is extremely important in PEC cell design. Recent work has shown that faradaic O₂ production is not achieved at WO₃ photoanodes in common aqueous electrolytes such as H₂SO₄, HClO₄, and HCl, with anion oxidation competing with water oxidation on the WO₃ surface.^{30–32} Further, Hill and Choi showed that WO₃ was not stable in many acidic electrolytes.³⁰ Solarska et al. achieved stable photocurrents for up to 14 h using a methane sulfonic acid electrolyte after an initial loss (over 1–2 h) of 20% of the

photocurrent for their nanostructured WO_3 electrodes.³³ We observed similar behavior for our films (Supporting Information Figure S7). However, this initial degradation complicated the comparison of samples over repeated short-term tests. As we were primarily interested in the bulk film properties and not the kinetics of oxidation processes at its surface, 0.1 M methanol was added as a hole scavenger for most testing. This facilitated stable, consistent behavior over repeated PEC tests. Methanol oxidation is significantly easier than water oxidation and takes part in current doubling,³⁴ so larger photocurrents were observed with its addition (Figure 3). Complementary

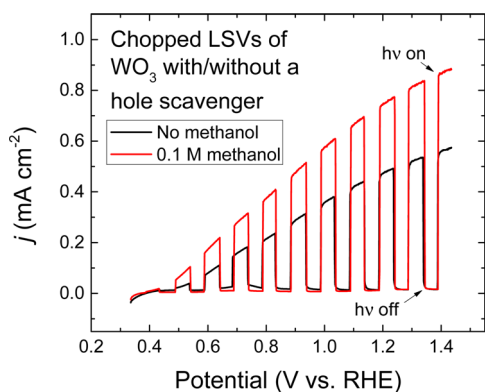


Figure 3. Chopped linear scan voltammograms (LSV) of undoped WO_3 in 1 M methanesulfonic acid with and without 0.1 M methanol as a hole scavenger under AM1.5G simulated solar light (100 mW cm^{-2}). The scan rate was 10 mV s^{-1} , and potential was scanned in the positive direction.

experiments without the addition of methanol showed the same trends (Supporting Information Figure S8a and b). Surprisingly, no oxygen bubbles were observed during ~ 1 h long tests in 1 M methanesulfonic acid (data in Supporting Information Figure S8b), suggesting a significant fraction of the photocurrent did not go toward water oxidation in this electrolyte. As previously mentioned, this is often the case for WO_3 photoanodes and highlights the need for oxygen evolution reaction electrocatalysts for this material,³⁵ which is a subject of further research in our laboratory.

The photocurrents achieved with our undoped WO_3 films (0.5 and 0.75 mA cm^{-2} at 1.23 V vs RHE with and without a hole scavenger, respectively) are comparable to other WO_3 films deposited by spray pyrolysis (SP), such as the work of Sun et al. (when their higher lamp intensity is taken into account).⁸ However, the performance of the samples deposited by SP is lower than other WO_3 films synthesized by sol-gel,^{33,34} RF sputtering,¹⁵ or electrodeposition³² under the same illumination conditions. We attribute this to two key differences between films grown by SP and those by other methods: the degree of nanostructuring and film thickness. The best performing WO_3 electrodes have features on the order of 50 nm , increasing the active surface area and minimizing carrier transport distances relative to the compact, rough microstructure (Figure 1) observed in our work. Further, nanometer sized features may scatter incident light, allowing the use of thinner, more efficient films ($\sim 2.4 \mu\text{m}$ or less compared to an average of $5 \mu\text{m}$) (Figure 1b). Incorporation of S and I into WO_3 photoelectrodes with advantageous morphologies either by optimizing the SP technique or by other synthesis methods would be an interesting avenue for future work.

The trends with increased S or I doping are shown in Figure 4. At very low S concentrations, photocurrents were improved

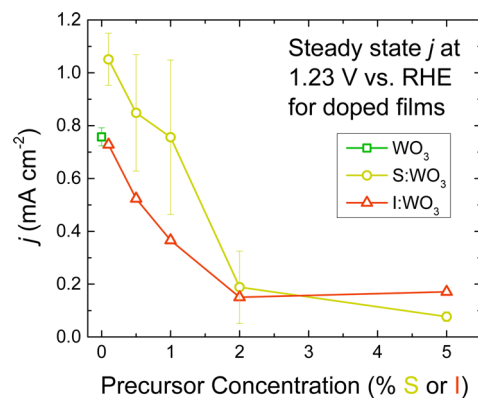


Figure 4. Steady state photocurrent under AM1.5G simulated solar light (100 mW cm^{-2}) vs initial sulfur and iodine precursor concentration. Points with error bars were constructed using the average of 3 films ± 1 standard deviation.

compared to undoped WO_3 but worsened with increasing sulfur. The large decrease in performance at 2% coincides with poorer crystallinity as seen in the XRD data (Supporting Information Figure S1). Film performance was variable, especially around 1% S: WO_3 , where a possible change in the incorporation mechanism may have occurred. Evidence for this will be provided in section 3.8.

As shown in Figure 5a, 0.1% S: WO_3 exhibited improved full spectrum and visible light photocurrents compared to undoped WO_3 . Incident photon conversion efficiency (IPCE) measurements showed increased efficiency at longer wavelengths. All S: WO_3 films showed a similar spectral profile (Supporting Information Figure S9) that is in agreement with the shift to longer wavelengths in the UV-vis absorption spectra (Figure 2). We note that the 0.1% S: WO_3 sample exhibited a slight IPCE improvement at wavelengths less than 400 nm (Figure 5b) and attribute this to variations in film thickness, and hence performance, as shown by the error bars in Figure 4. For a full discussion, see Section S3.1 in the Supporting Information. A typical power density spectrum for IPCE testing is located in the Supporting Information (Figure S10). Integration of the IPCE values with respect to the AM1.5G reference spectrum (ASTM G-173)³⁶ overestimated the photocurrent by up to 30% but showed the same trends as seen for photocurrents obtained with the solar simulator (Supporting Information Tables S1 and S2). This overestimation may arise due to a decreased carrier recombination rate at low light intensity.

With increasing I incorporation, overall photocurrent decreased (Figure 4), possibly due to an increased number of recombination sites due to a higher concentration of defects. Despite absorbing substantially more visible light, 0.1% I: WO_3 exhibited only a slight increase in the visible light contribution to the total photocurrent (Figure 5a), which occurred with a corresponding decrease in IPCE at wavelengths less than 400 nm (Figure 5b). The spectral shape was maintained even as increased I incorporation hurt overall PEC performance (Supporting Information Figure S11).

3.5. ToF-SIMS. To determine the amounts and distributions of S and I in the films, sequential ToF-SIMS and XPS analyses were carried out. The samples used had not been previously PEC tested to avoid contamination with the sulfur-containing

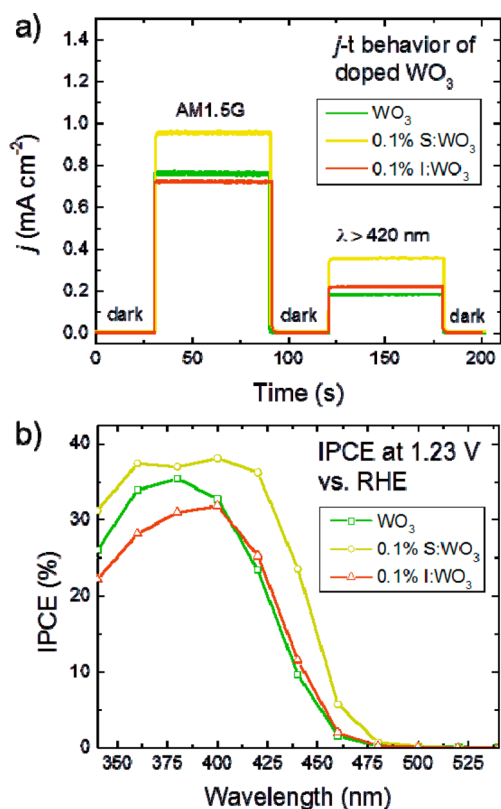


Figure 5. (a) Photocurrent–time ($j-t$) data under AM1.5G simulated solar light (100 mW cm^{-2}) and with a long pass filter. The electrolyte was 1 M methane sulfonic acid with 0.1 M methanol. Complementary $j-t$ data without methanol showed the same trend (Figure S8a in the Supporting Information). (b) IPCE vs wavelength at 1.23 V vs RHE. The electrolyte in both cases was 1 M methane sulfonic acid with 0.1 M methanol.

electrolyte. The selection of suitable marker ions is discussed in the Supporting Information (Section S4).

Depth profiling on different areas of the samples indicated different thicknesses. As shown in Figure 1, the film is extremely rough; thus, it was not practical to convert the sputtering time to a film depth. To ensure a fair analysis of the bulk film in all cases, we compared the depth profiles up to 2500 s of sputtering time, where signals from FTO substrate emerged in the thinnest areas.

Figures 6a and b illustrate the depth profiles for representative S:WO₃ and I:WO₃ samples. The sulfur distribution was uniform throughout the films (Figure 6a) and qualitatively agreed with the trend in precursor concentrations, that is, the higher the S concentration in precursor, the more S in the resulting film. As shown in Figure 6a (tabulated in Table S3 in the Supporting Information), scaling was relatively close until 2%, where there was a jump in S concentration. After this point, saturation of S in the WO₃ lattice seems to be occurring.

Conversely, the I distribution varied as a function of sputtering depth with a maximum at the surface that tailed off through the film. We speculate that this concentration profile was caused by the pulsed nature of the spray pyrolysis synthesis and volatile nature of iodine at the deposition temperature ($\sim 250 \text{ }^\circ\text{C}$). After each deposition cycle, the as-deposited film was left at the hot plate temperature to allow for solvent evaporation, during which iodine left the sample. The

final layers near the top of the film spent the least amount of time on the hot plate and so retained the most iodine. The concentration of I scaled well with the initial concentration in the precursor but saturated after 1% near the bottom of the films (after 1000 s in Figure 6b).

3.6. XPS. XPS was used to quantify the concentrations and charge states of the dopants. W 4f and O 1s regions agreed well with reported tungsten trioxide XPS spectra,^{37,38} with peaks at 35.7 eV (4f_{7/2}) and 530.5 eV, respectively (Figure 6c and d). These indicate the presence of W⁶⁺ and O²⁻. Fitting of the W 4f region showed the correct peak splitting (2.2 eV) and area ratio (0.75) between 4f_{7/2} and 4f_{5/2} peaks; thus, only the 6+ oxidation state of tungsten was observed. The shoulder at higher B.E. on the main O 1s peak (Figure 6d) has been observed in many transition metal oxides and is attributed to either defective oxygen sites^{39,40} or surface hydroxides.

Due to the low concentration of S and I in the doped samples, heavily doped samples (20% S:WO₃ and 2% I:WO₃) were used for XPS analysis of the chemical speciation within the films. With the incorporation of S and I, we saw no significant changes in the W 4f and O 1s regions compared to undoped WO₃. The W:O atomic ratio was ~ 3 for all samples.

Despite our best efforts and intense scan conditions (1.5 s dwell time, 16 sweeps), we did not observe a sulfur signal in the bulk of the 20% S:WO₃ sample (correspondingly, lower concentration samples also had no detectable signal). There was a surface concentration of S⁶⁺ (Supporting Information Figure S12a), which has been observed in other reports.²⁰ This peak disappeared after light Ar⁺ sputtering (Supporting Information Figure S12b); therefore, we attribute it to surface sulfate species. Clearly, it is not the same as the bulk S observed in the ToF-SIMS data (Figure 6a), which was uniform throughout the film. Therefore, we could not assign charge states or quantify the sulfur concentration for the S:WO₃ films. We could, however, estimate an upper limit of the concentration by fitting the instrumental noise. This yielded an upper limit for sulfur doping of $\sim 0.1\%$ compared to 20%, indicating a very low incorporation level relative to the precursor concentrations.

The I 3d_{5/2} peak was located at 619.5 eV (Figure 6e) corresponding to I in the 1-oxidation state.²¹ Combined ToF-SIMS and XPS were used to quantify the concentration of I in the films. This procedure is detailed in Section S5.3 in the Supporting Information. Figure 6b shows a maximum concentration of 0.3% relative to the oxygen sites, on the same order as the incorporation levels for the S:WO₃ samples. These analyses show that large excesses of both of these impurities were required to incorporate them into WO₃, even in small amounts. The difficulties detecting sulfur by XPS is likely due to its low relative sensitivity factor compared to iodine (0.668 for S 2p vs 10.343 for I 3d) and the very low concentrations present.

3.7. Raman Spectroscopy. Raman spectroscopy was used to probe changes in the WO₃ bonding environment due to sulfur or iodine incorporation. Undoped WO₃ showed only characteristic peaks for the monoclinic phase (Figure 7).^{41,42} Note that this spectrum is quite complex: 48 Raman modes are active,⁴¹ and only the main peaks have been assigned in the literature.

Upon sulfur incorporation (2% and above), shifts to lower wavenumbers of the modes at 273, 717, and 807 cm⁻¹ and peak broadening occurred (Figure 7 and Supporting Information Figure S14). These bands correspond to stretching modes of

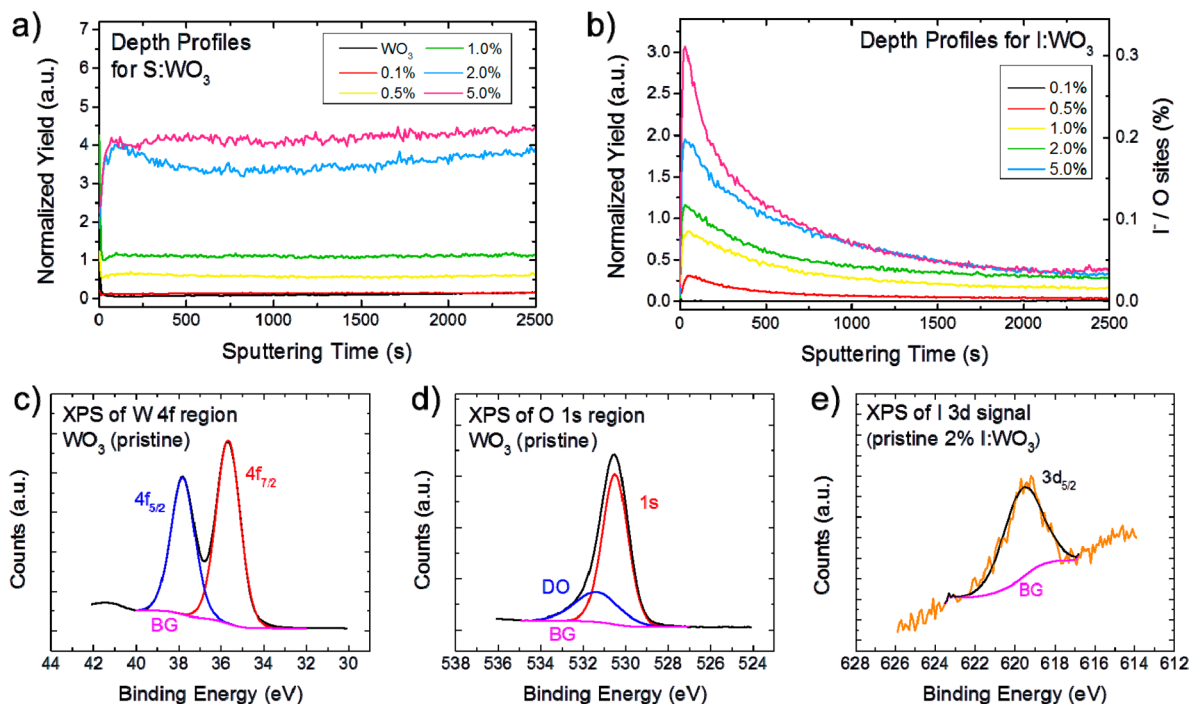


Figure 6. (a) ToF-SIMS depth profiles of S:WO₃ showing the fraction of the marker ions (S⁻/¹⁸⁰WO₃) vs sputtering time for each film. (b) ToF-SIMS depth profiles of I:WO₃ films showing the fraction of the marker ions (I^O/¹⁸⁰WO₃) vs sputtering time on the left y axis. The normalized yield was converted to the percentage of I⁻ of total O sites using XPS data on the right y axis, where O sites = 3*W⁶⁺ concentration from the XPS data, assuming fully oxidized WO₃. This was performed for comparison to the starting precursor concentrations. XPS data and fitting for pristine, undoped WO₃ (c) W 4f region, (d) O 1s region, and (e) pristine 2% I:WO₃, I 3d region. OH/DO: hydroxide/defect oxide, BG: background.

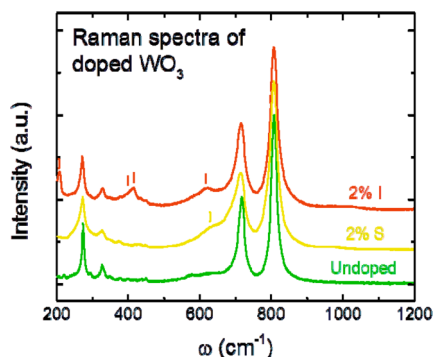


Figure 7. Raman spectra of undoped and doped films. Only traces for undoped, 2% S:WO₃ and 2% I:WO₃ films are shown for simplicity. Vertical ticks indicate peaks either not present or weaker in the undoped WO₃ spectrum. Spectra for all samples can be located in the Supporting Information.

the W–O bonds, and a shift to lower wavenumbers suggests a heavier atom such as sulfur has replaced the oxygen.⁴³ Peak broadening in Raman spectra is associated with poorer crystallinity, as seen in the XRD data (Supporting Information Figure S1). It was difficult to assign the broad peak at ~630 cm⁻¹, as though this slight shoulder is present in the undoped samples; it is very weak and has not been previously assigned. It does not line up with Raman bands in examples of W–S or S–O bonding as in tungsten disulfide⁴⁴ or sulfur dioxide.^{45,46} A candidate feature has been observed in aqueous sulfate solutions: the deformation of the S₂O₅²⁻ ion,⁴⁶ but none of the other modes for this ion were present in our spectra. Additionally, a similar feature has been seen in Raman spectra for WO₃ cationically doped with Sn and Si but was not

assigned.⁴⁷ Therefore, we cannot conclusively determine whether only sulfur substitution on the O site or a combination of cation and anion sulfur substitution occurs in these heavily doped samples. Surprisingly, we did not observe peak shifts up to 1% S:WO₃ (Supporting Information Figure S14) because either the very low concentrations could not be detected by Raman or the nature of sulfur incorporation in the WO₃ lattice was not substitutional at concentrations less than 2%.

Increasing iodine incorporation resulted in gradual peak shifts to lower wavenumber and broadening (Figure 7 and Supporting Information Figure S15), which we attribute to substitution of I on the O site and a lower degree of crystalline perfection. Several auxiliary peaks became more pronounced with I incorporation, those at ~207, 400, 415, and 615 cm⁻¹ (Figure 7). As previously mentioned, the Raman spectra of monoclinic WO₃ is quite complex, so it was difficult to determine whether these are existing peaks whose intensity has increased or new modes due to iodine in the WO₃ lattice (Supporting Information Figure S16). As the intensity of these peaks tracks with increasing I content, we tentatively assign to them new W–I bonding modes. There is a lack of tungsten oxyiodide compounds in the literature and, hence, no reference Raman patterns. Theoretical calculations will be invaluable in elucidating the nature of these peaks in both the S:WO₃ and I:WO₃ samples.

3.8. Incorporation Mechanism. Monoclinic WO₃ (space group P2₁/n, *a* = 7.327 Å, *b* = 7.564 Å, *c* = 7.727 Å, β = 90.49°)⁴⁸ adopts a distorted cubic ReO₃ structure, closely related to the cubic perovskite (AMO₃) structure but without a cation on the A site. It consists of tilted edge-sharing WO₆ octahedra (Figure 8a). Several possible cases exist for dopant incorporation in the lattice: (i) interstitially, (ii) intercalation in

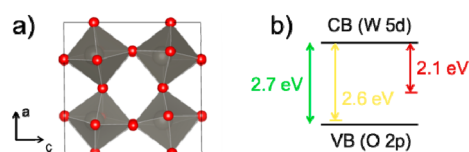


Figure 8. (a) Schematic of the monoclinic WO_3 structure, illustrating edge-sharing WO_6 units (gray) and oxygen atoms (red) created with VESTA software.⁵³ (Not to scale.) (b) Simplified band diagram showing the suggested locations of midgap impurity bands.

the “empty” A site between the WO_6 units, (iii) substitutionally for W, or (iv) for O.

Sulfur. Because bulk S could not be detected, even in heavily doped films, XPS could not be used to provide evidence for the location of S atoms. Li et al. showed the presence of S^{6+} on the surface of their S:WO₃ powders and associated it with the substitution of W^{6+} by S^{6+} .²⁰ It is worth noting that this has been observed in the case of S:TiO₂, where sulfur has been detected in the 2−,⁴⁹ 4+,⁵⁰ and 6+⁵¹ oxidation states, indicating both anionic and cationic substitutions are possible. The cases of 2− and 4+ have been studied by DFT, where substitution on either site did not change the electronic density of states significantly,⁵² that is, the sulfur 3p orbitals form impurity states close the valence band edge of TiO₂.

As mentioned in Section 3.7, no differences between the undoped and S:WO₃ samples were observed until 2%, after which O—and possibly W—substitution occurred. Considering theoretical calculations for S on O site substitution in S:WO₃^{18,19} and by analogy with cation doped S:TiO₂,⁵² we suggest that at these higher dopant concentrations, a relatively shallow defect state is formed ~ 0.1 eV above the valence band (Figure 8b), which caused increased visible light absorption. At these higher levels of incorporation, the crystalline quality of the lattice has been degraded (broadening of XRD and Raman peaks) leading to lower PEC performance.

Below 1% S:WO₃, no sulfur was detected by XPS or Raman up to 1200 cm^{-1} . This prompted us to look at other incorporation options, such as an oxidized sulfur compound (e.g., SO₂) in the space between the WO_6 octahedra, in which case, Raman modes consistent with S–O bonding should be present. As an example, stable N₂ intercalation has been observed in monoclinic WO₃.⁵⁴ However, we saw no differences in the Raman spectra up to 4500 cm^{-1} . Though we cannot comment on the location of sulfur in the lightly doped samples, there are large changes from 1 to 2% S:WO₃ in the XRD spectra (Supporting Information Figure S1), Raman (Supporting Information Figure S14), UV–vis (Supporting Information Figure S4, inset), ToF-SIMS (Figure 6a), and PEC data (Figure 4). It is possible that the incorporation mechanism at low concentrations may be different than the substitution seen in the heavily doped case, though the UV–vis spectra (Supporting Information Figure S4) would suggest that in both scenarios a shallow defect state is created. Sensitive analytical techniques, for example, solid state NMR, hard X-ray absorption spectroscopy, or neutron scattering may help understand the role of sulfur at these low concentrations but are out of the scope of this study.

Iodine. Raman spectroscopy indicated I substituted for O and as only I[−] was present the XPS spectra, we conclude that this ion substitutionally replaced O^{2−} in WO₃. We would expect this substitution to be quite destructive to the lattice as I[−] is much larger than O^{2−} (2.2 Å vs 1.4 Å for 6-fold

coordination).⁵⁵ Additionally, I[−] should act as an electron donor, possibly resulting in W^{6+} vacancies or reduced W sites so that the excess charge is balanced, further lowering the crystalline quality. No peak broadening was observed in XRD spectra but was observed using Raman spectroscopy with progressive I doping. UV–vis spectroscopy indicates that iodine forms a deep impurity band, ~ 0.6 eV above the valence band maximum (Figure 8b). The combination of this deep trap acting as a recombination center and disruption of the crystal lattice explains the poorer PEC performance of the I:WO₃ films.

4. CONCLUSIONS

In summary, we synthesized films of sulfur or iodine incorporated WO₃ with the aim to improve its visible light harvesting ability and PEC performance. Red shifts of the absorption spectra were observed with S and I incorporation (from ~ 2.7 to 2.6 and 2.1 eV respectively). S:WO₃ samples exhibited better PEC performance at low S concentrations but worsened with increasing S addition. PEC and IPCE data showed that this initial improvement was driven by improved collection efficiency at longer wavelengths. Conversely, photocurrent decreased at all levels of I addition. IPCE measurements for these films showed only a marginal increase in efficiency at longer wavelengths, indicating that the extra absorbed photons did not contribute significantly to the photocurrent. ToF-SIMS was used to detect the very small levels of impurities and revealed a uniform concentration of S throughout S:WO₃ films, but a decreasing I concentration from the surface in the I:WO₃ samples. Raman and XPS showed that S and I substituted for oxygen, but in the case of S, other pathways—such as intercalation and cation substitution—could not be ruled out. In the case of S:WO₃, the relatively shallow impurity state allowed greater visible light absorption without compromising the quality of the crystal lattice at low concentrations, whereas incorporation of iodine created a deep impurity band, negatively affecting the performance at all concentrations investigated in this study. Nonmetal doping of metal oxides is a contentious subject in the literature and our study highlights that advanced characterization techniques and theoretical calculations will be vital in understanding these new materials.

■ ASSOCIATED CONTENT

Supporting Information

XRD, UV–vis, Raman and PEC testing for all films, Tauc analyses, long-term j – t testing, and XPS analyses. This material is available free of charge via the Internet at <http://pubs.acs.org>.

■ AUTHOR INFORMATION

Corresponding Author

*C. B. Mullins. E-mail: mullins@che.utexas.edu.

Notes

The authors declare no competing financial interest.

■ ACKNOWLEDGMENTS

The authors gratefully acknowledge the U.S. Department of Energy (DOE) Grant DE-FG02-09ER16119 and Welch Foundation Grant F-1436. Additionally, we thank the National Science Foundation grants DMR-0618242 and DMR-0923096 used to purchase the Kratos XPS and ION-TOF TOF.SIMS 5 instruments, respectively. J.-F.L. was supported as part of EFree, an Energy Frontier Research Center funded by the DOE

Office of Science, Office of Basic Energy Sciences, under Award DE-SC0001057. A.J.E.R. thanks W.D. Chemelewski for useful discussions. Finally, we acknowledge C.J. Stolle and B.A. Korgel for their help with diffuse reflectance UV-vis spectroscopy measurements.

REFERENCES

- (1) In this paper, "WO₃" will refer to the high temperature monoclinic phase of WO₃ (γ -WO₃) as opposed to the low temperature monoclinic form (ϵ -WO₃).
- (2) Grätzel, M. *Nature* **2001**, *414*, 338.
- (3) Brillet, J.; Yum, J.-H.; Cornuz, M.; Hisatomi, T.; Solarska, R.; Augustynski, J.; Graetzel, M.; Sivula, K. *Nat. Photonics* **2012**, *6*, 824.
- (4) Miller, E. L.; Paluselli, D.; Marsen, B.; Rocheleau, R. E. *Sol. Energy Mater. Sol. Cells* **2005**, *88*, 131.
- (5) Chen, Z.; Jaramillo, T. F.; Deutsch, T. G.; Kleiman-Shwarscstein, A.; Forman, A. J.; Gaillard, N.; Garland, R.; Takanabe, K.; Heske, C.; Sunkara, M. J. *Mater. Res.* **2010**, *25*, 3.
- (6) Maruthamuthu, P.; Ashokkumar, M. *Sol. Energy Mater.* **1988**, *17*, 433.
- (7) Baeck, S. H.; Jaramillo, T. F.; Braendli, C.; McFarland, E. W. *J. Comb. Chem.* **2002**, *4*, 563.
- (8) Sun, Y.; Murphy, C. J.; Reyes-Gil, K. R.; Reyes-Garcia, E. A.; Thornton, J. M.; Morris, N. A.; Raftery, D. *Int. J. Hydrogen Energy* **2009**, *34*, 8476.
- (9) Zheng, H.; Tachibana, Y.; Kalantar-zadeh, K. *Langmuir* **2010**, *26*, 19148.
- (10) Su, J.; Guo, L.; Bao, N.; Grimes, C. A. *Nano Lett.* **2011**, *11*, 1928.
- (11) Hong, S. J.; Lee, S.; Jang, J. S.; Lee, J. S. *Energy Environ. Sci.* **2011**, *4*, 1781.
- (12) Sivula, K.; Formal, F. L.; Grätzel, M. *Chem. Mater.* **2009**, *21*, 2862.
- (13) Chatchai, P.; Murakami, Y.; Kishioka, S.-y.; Nosaka, A. Y.; Nosaka, Y. *Electrochim. Acta* **2009**, *54*, 1147.
- (14) He, H.; Berglund, S. P.; Xiao, P.; Chemelewski, W. D.; Zhang, Y.; Mullins, C. B. *J. Mater. Chem. A* **2013**, *1*, 12826.
- (15) Cole, B.; Marsen, B.; Miller, E.; Yan, Y.; To, B.; Jones, K.; Al-Jassim, M. J. *Phys. Chem. C* **2008**, *112*, 5213.
- (16) Liu, Y.; Li, Y.; Li, W.; Han, S.; Liu, C. *Appl. Surf. Sci.* **2012**, *258*, 5038.
- (17) Nah, Y.-C.; Paramasivam, I.; Hahn, R.; Shrestha, N. K.; Schmuki, P. *Nanotechnology* **2010**, *21*, 105704.
- (18) Migas, D.; Shaposhnikov, V.; Rodin, V.; Borisenko, V. *J. Appl. Phys.* **2010**, *108*, 093713.
- (19) Wang, F.; Di Valentin, C.; Pacchioni, G. *J. Phys. Chem. C* **2012**, *116*, 8901.
- (20) Li, W.; Li, J.; Wang, X.; Chen, Q. *Appl. Surf. Sci.* **2012**, *263*, 157.
- (21) Tojo, S.; Tachikawa, T.; Fujitsuka, M.; Majima, T. *J. Phys. Chem. C* **2008**, *112*, 14948.
- (22) Hahn, N. T.; Hoang, S.; Self, J. L.; Mullins, C. B. *ACS Nano* **2012**, *6*, 7712.
- (23) Hahn, N. T.; Self, J. L.; Mullins, C. B. *J. Phys. Chem. Lett.* **2012**, *3*, 1571.
- (24) Miller, D.; Biesinger, M.; McIntyre, N. *Surf. Interface Anal.* **2002**, *33*, 299.
- (25) Biesinger, M. C.; Payne, B. P.; Lau, L. W.; Gerson, A.; Smart, R. S. C. *Surf. Interface Anal.* **2009**, *41*, 324.
- (26) Wojdyr, M. *J. Appl. Crystallogr.* **2010**, *43*, 1126.
- (27) Light, T. S. *Anal. Chem.* **1972**, *44*, 1038.
- (28) Enesca, A.; Duta, A.; Schoonman, J. *Thin Solid Films* **2007**, *515*, 6371.
- (29) Hao, J.; Studenikin, S.; Cocivera, M. *J. Appl. Phys.* **2001**, *90*, 5064.
- (30) Hill, J. C.; Choi, K.-S. *J. Phys. Chem. C* **2012**, *116*, 7612.
- (31) Mi, Q.; Coridan, R. H.; Bruntschwig, B. S.; Gray, H. B.; Lewis, N. S. *Energy Environ. Sci.* **2013**, *6*, 2646.
- (32) Mi, Q.; Zhanaidarova, A.; Bruntschwig, B. S.; Gray, H. B.; Lewis, N. S. *Energy Environ. Sci.* **2012**, *5*, 5694.
- (33) Solarska, R.; Jurczakowski, R.; Augustynski, J. *Nanoscale* **2012**, *4*, 1553.
- (34) Santato, C.; Ulmann, M.; Augustynski, J. *J. Phys. Chem. B* **2001**, *105*, 936.
- (35) Seabold, J. A.; Choi, K.-S. *Chem. Mater.* **2011**, *23*, 1105.
- (36) NREL. Reference Solar Spectral Irradiance: ASTM G-173. <http://rredc.nrel.gov/solar/spectra/am1.5/ASTMG173/ASTMG173.html> (accessed October, 2013).
- (37) Yous, B.; Robin, S.; Donnadieu, A.; Dufour, G.; Maillot, C.; Roulet, H.; Senemaud, C. *Mater. Res. Bull.* **1984**, *19*, 1349.
- (38) Blackman, C. S.; Parkin, I. P. *Chem. Mater.* **2005**, *17*, 1583.
- (39) Biesinger, M. C.; Lau, L. W.; Gerson, A. R.; Smart, R. S. C. *Appl. Surf. Sci.* **2010**, *257*, 887.
- (40) Biesinger, M. C.; Payne, B. P.; Grosvenor, A. P.; Lau, L. W.; Gerson, A. R.; Smart, R. S. C. *Appl. Surf. Sci.* **2011**, *257*, 2717.
- (41) Salje, E. *Acta Crystallogr., Sect. A: Cryst. Phys., Diffr., Theor. Gen. Crystallogr.* **1975**, *31*, 360.
- (42) Daniel, M.; Desbat, B.; Lassegues, J.; Gerand, B.; Figlarz, M. *J. Solid State Chem.* **1987**, *67*, 235.
- (43) Vandenabeele, P. *Practical Raman Spectroscopy: An Introduction*; John Wiley & Sons: Hoboken, NJ, 2013.
- (44) Zabinski, J.; Donley, M.; Prasad, S.; McDevitt, N. *J. Mater. Sci.* **1994**, *29*, 4834.
- (45) Anderson, A.; Savoie, R. *Can. J. Chem.* **1965**, *43*, 2271.
- (46) Davis, A.; Chatterjee, R. *J. Solution Chem.* **1975**, *4*, 399.
- (47) Solarska, R.; Alexander, B. D.; Braun, A.; Jurczakowski, R.; Fortunato, G.; Stiefel, M.; Graule, T.; Augustynski, J. *Electrochim. Acta* **2010**, *55*, 7780.
- (48) Vogt, T.; Woodward, P. M.; Hunter, B. A. *J. Solid State Chem.* **1999**, *144*, 209.
- (49) Umebayashi, T.; Yamaki, T.; Itoh, H.; Asai, K. *Appl. Phys. Lett.* **2002**, *81*, 454.
- (50) Ohno, T.; Akiyoshi, M.; Umebayashi, T.; Asai, K.; Mitsui, T.; Matsumura, M. *Appl. Catal., A* **2004**, *265*, 115.
- (51) Yu, J. C.; Ho, W.; Yu, J.; Yip, H.; Wong, P. K.; Zhao, J. *Environ. Sci. Technol.* **2005**, *39*, 1175.
- (52) Matsushima, S.; Takehara, K.; Yamane, H.; Yamada, K.; Nakamura, H.; Arai, M.; Kobayashi, K. *J. Phys. Chem. Solids* **2007**, *68*, 206.
- (53) Momma, K.; Izumi, F. *J. Appl. Crystallogr.* **2011**, *44*, 1272.
- (54) Mi, Q.; Ping, Y.; Li, Y.; Cao, B.; Bruntschwig, B. S.; Khalifah, P. G.; Galli, G. A.; Gray, H. B.; Lewis, N. S. *J. Am. Chem. Soc.* **2012**, *134*, 18318.
- (55) Shannon, R. *Acta Crystallogr., Sect. A: Cryst. Phys., Diffr., Theor. Gen. Crystallogr.* **1976**, *32*, 751.